The Astrophysical Journal, 810:69 (9pp), 2015 September 1 doi:10.1088/0004-637X/810/1/69

PROPER MOTIONS IN TERZAN 5: MEMBERSHIP OF THE MULTI-IRON SUBPOPULATIONS AND FIRST CONSTRAINT ON THE ORBIT*

D. Massari[1,2], E. Dalessandro[3], F. R. Ferraro[3], P. Miocchi[3], A. Bellini[4], L. Origlia[1], B. Lanzoni[3], R. M. Rich[5], and A. Mucciarelli[3]
[1] INAF-Osservatorio Astronomico di Bologna, via Ranzani 1, I-40127, Bologna, Italy
[2] Kapteyn Astronomical Institute, University of Groningen, PO Box 800, 9700 AV Groningen, The Netherlands
[3] Dipartimento di Fisica e Astronomia, Università degli Studi di Bologna, v.le Berti Pichat 6/2, I-40127 Bologna, Italy
[4] Space Telescope Science Institute, 3700 San Martin Drive, Baltimore, MD 21218, USA
[5] Department of Physics and Astronomy, Math-Sciences 8979, UCLA, Los Angeles, CA 90095-1562, USA
Received 2015 June 23; accepted 2015 July 9; published 2015 September 1

ABSTRACT

By exploiting two sets of high-resolution images obtained with the *Hubble Space Telescope* Advanced Camera for Surveys/Wide Field Channel over a baseline of ∼10 years, we have measured relative proper motions (PMs) of ∼70,000 stars in the stellar system Terzan 5. The results confirm the membership of the three subpopulations with different iron abundances discovered in the system. The orbit of the system has been derived from a first estimate of its absolute PM, obtained by using bulge stars as a reference. The results of the integration of this orbit within an axisymmetric Galactic model exclude any external accretion origin for this cluster. Terzan 5 is known to have chemistry similar to the Galactic bulge; our findings support a kinematic link between the cluster and the bulge, further strengthening the possibility that Terzan 5 is the fossil remnant of one of the pristine clumps that originated the bulge.

Key words: astrometry – Galaxy: bulge – globular clusters: individual (Terzan 5) – proper motions

1. INTRODUCTION

Terzan 5 is a stellar system located at the edge of the inner bulge of the Galaxy ($l = 3.^{\circ}8395$, $b = 1.^{\circ}6868$) at a distance of 5.9 kpc from the Sun (Valenti et al. 2007). Because of the large and spatially variable extinction in that region of the sky (Massari et al. 2012), observations of this system are extremely challenging, particularly in the optical bands. This is why the complex nature of Terzan 5 has been revealed only recently by means of high-resolution infrared (IR) photometric (Ferraro et al. 2009) and spectroscopic (see Origlia et al. 2011) observations of its stellar populations with the ESO-Very Large Telescope and Keck telescopes. These studies revealed that Terzan 5 hosts two distinct populations with significantly different iron content (Δ[Fe/H] = 0.5 dex), different levels of α-element enhancement, and no evidence of the anticorrelation among light elements commonly observed in globular clusters (GCs; e.g., Carretta 2014 and references therein). The radial distribution of the two populations is incompatible with that of field stars. In addition, the metal-rich component has been found to be significantly more centrally concentrated than the metal-poor one (Lanzoni et al. 2010). Also, the two populations have been found to share the same mean radial velocities (Massari et al. 2014a and references therein) and the same center of gravity (Lanzoni et al. 2010). All of these features add weight to the membership of these populations. However, even with the spatial distribution and radial velocity membership secure, their actual membership has been questioned (e.g., Willman & Strader 2012) because of the strong field-star contamination affecting many GCs in the direction of the bulge (see Valenti et al. 2007, 2010). Recently, also a third, metal-poor and α-enhanced population has been discovered (Origlia et al. 2013). Although small in number, such a component has the same systemic radial velocity as the cluster (Origlia et al. 2013), and it has survived all statistical decontamination tests (see the discussion in Massari et al. 2014b).

In order to properly separate genuine Terzan 5 stars from foreground and background sources, we measured high-precision relative proper motions (PMs) of individual stars in the direction of the system by exploiting the superb astrometric accuracy of the *Hubble Space Telescope* (*HST*) (see, e.g., Anderson & van der Marel 2010; Dalessandro et al. 2013; Massari et al. 2013; Bellini et al. 2014; Watkins et al. 2015, and references therein). Here we report on the results of this PM study, which also confirms the membership of the three iron groups.

This paper is organized as follows. In Section 2 we present the data set used, and in Section 3 we describe the techniques adopted to measure PMs. Finally, we present the results of our work in Section 4, and we summarize the conclusions in Section 5.

2. OBSERVATIONS AND DATA REDUCTION

In the context of a multiwavelength program aimed at studying the photometric properties of the multi-iron subpopulations of Terzan 5, we have acquired (GO12933, PI: Ferraro) a set of optical and near-infrared (NIR) images of the system by using the Wide Field Channel (WFC) of the Advanced Camera for Surveys (ACS) and the IR channel of the Wide Field Camera 3 (WFC3) on board the *HST*. In the following we will focus on the optical data set only because the subject of the present paper is the accurate measure of the stellar PMs, and the larger pixel scale of the WFC3 IR camera detector ($\sim 0.''13$ pixel^{-1}) makes the secured IR images unsuitable for this purpose. The ACS/WFC is made up of two 2048 × 4096 pixel detectors with a pixel scale of $\sim 0.''05$ pixel^{-1} and separated by a gap of about 50 pixels. The total field of view (FOV) is $\sim 200'' \times 200''$. The optical data set

* Based on observations (GO12933, GO9799) with the NASA/ESA *Hubble Space Telescope*, obtained at the Space Telescope Science Institute, which is operated by AURA, Inc., under NASA contract NAS 5-26555.

consists of 5 × 365 s images in F606W, 5 × 365 s images in F814W, and one short exposure per filter (50 and 10 s, respectively). The observations were performed on 2013 August 18 and provided an optimal second-epoch data set for PM measures.

The first-epoch images (GO9799, PI: Rich) consist of two deep (340 s) exposures in the F606W and F814W filters and one short exposure (10 s) in the F814W filter, also acquired with the ACS/WFC. This data set was used to construct the deepest optical color–magnitude diagram (CMD) of Terzan 5 (see Ferraro et al. 2009; Lanzoni et al. 2010). The images were acquired on 2003 September 9. Thus, the combination of the two optical data sets provides a total time baseline of ∼9.927 years.

3. RELATIVE PMs

The analysis has been performed on _flc images, which have been flat-fielded, bias-subtracted, and corrected for charge transfer efficiency (CTE) losses by the standard *HST* calibration pipeline (CALACS) adopting the pixel-based correction described in Anderson & Bedin (2010) and Ubeda & Anderson (2012). The procedure used to derive relative PMs is described in detail in Massari et al. (2013). Here we provide only a brief description of the main steps of the analysis. The first step consists of the photometric reduction of each individual exposure of the two epochs with the publicly available program img2xym_WFC.09×10 (Anderson & King 2006; Anderson et al. 2008). This program uses a filter-dependent library of spatially varying point-spread function (PSF) models plus a single time-dependent perturbation PSF to account for focus changes or spacecraft breathing. The final output is a catalog with instrumental positions and magnitudes for a sample of sources above a given flux threshold in each exposure. Star positions were then corrected in each catalog for geometric distortion by means of the solution provided by Anderson (2007).

Figure 1 shows the ($m_{\rm F606W}$, $m_{\rm F606W}-m_{\rm F814W}$) CMD of Terzan 5 using the second-epoch data set (Figure 1). In particular, for stars fainter than $m_{\rm F606W}\simeq 20.7$ mag, which is the saturation limit of the deep images (solid gray line in Figure 1), all stars detected in at least three (out of five) deep single exposures per filter are plotted. Following the standard procedure (Lanzoni et al. 2007; Dalessandro et al. 2008), for each star, the magnitudes obtained from each single exposure in each filter were first homogenized, then averaged. The mean and standard deviation were finally adopted as the instrumental magnitude and photometric error, respectively (see Ferraro et al. 1991, 1992). For $m_{\rm F606W} < 20.7$ mag, we considered only stars measured in both of the short exposures, which saturate at $m_{\rm F606W}\simeq 19.1$ mag (dashed gray line in Figure 1). The instrumental magnitudes have been calibrated onto the Johnson photometric system using the stars in common with the catalog of Lanzoni et al. (2010). As apparent from the figure, the evolutionary sequences of Terzan 5 are clearly distinguishable although strongly affected by differential reddening. The main sequence extends for almost 4 mag below the turnoff. A blue sequence is visible at $m_{\rm F606W} < 24.5$ mag and $(m_{\rm F606W}-m_{\rm F814W}) < 3.6$ mag, and it remains well separated from the cluster red giant branch (RGB). This sequence is likely populated by young disk stars.

The second step in determining relative PMs is to astrometrically relate each exposure to a distortion-free

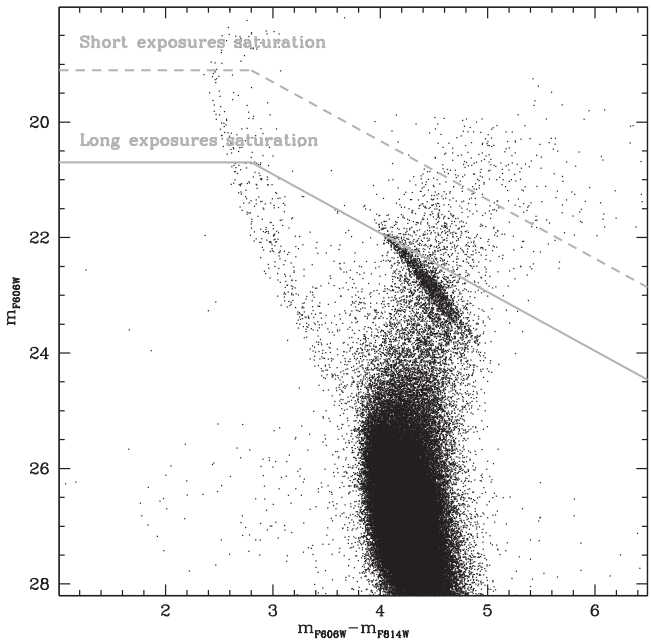

Figure 1. The ($m_{\rm F606W}$, $m_{\rm F606W}-m_{\rm F814W}$) CMD of Terzan 5. All of the cluster evolutionary sequences are broadened because of the differential reddening effect. A bright, blue sequence is clearly separated from the cluster sequences, and it is likely composed of young field stars. The magnitude saturation limits of the short and long exposures are marked with the dashed and solid lines, respectively.

reference frame, which from now on we will refer to as the *master frame*. Since no high-resolution astrometry other than that coming from these data sets is available, we defined as the master frame the catalog obtained from the combination of all of the second-epoch, single-exposure catalogs corrected for geometric distortion. In this way, the master frame is composed only of stars with at least 10 position measurements (five for each filter). We then applied a counterclockwise rotation of 91.°163 in order to give to the master frame the same orientation as the absolute reference frame defined by the Two Micron All Sky Survey (2MASS) catalog (see Lanzoni et al. 2010). We then transformed the measured position of each star in each exposure into the *master frame* by means of a six-parameter linear transformation. In order to maximize the accuracy, the transformations have been computed using only high signal-to-noise ($m_{\rm F606W} < 24$) and unsaturated sources that could be considered likely cluster members according to their position in the CMD. Also, in order to minimize the effects of CTE- and distortion-correction residuals, we treated each chip separately. At the end of the procedure, for each star we have up to three first-epoch position measurements and up to 12 second-epoch positions on the master frame. To estimate the relative PM of each star, we computed the median positions in the first and in the second epoch by applying a 3σ clipping algorithm. The difference between the two median positions gives the star's displacement over $\Delta T = 9.927$ years. Since for stars brighter than $m_{\rm F606W}\simeq 20.7$ one first-epoch and two second-epoch positions were available, we adopted the single position measured in the first epoch and the mean between the two positions measured in the second epoch. The errors in each

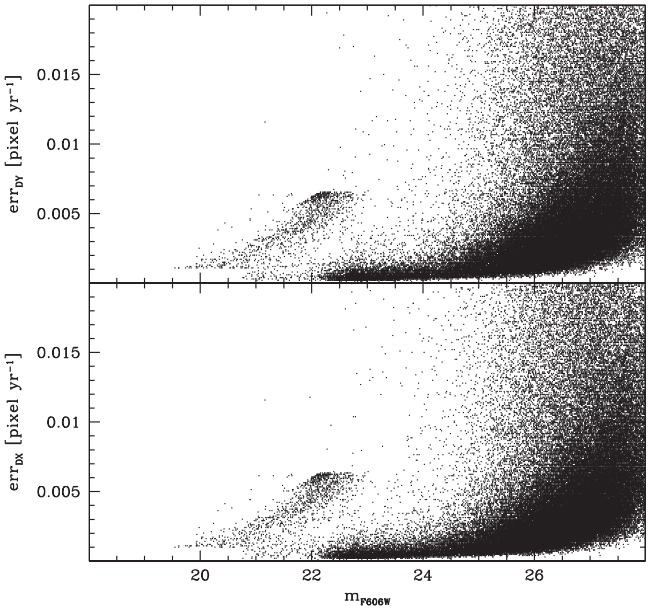

Figure 2. Uncertainties in the X and Y displacements in units of pixel yr^{-1}. Bright, well-measured stars have displacement errors typically smaller than 0.007 pixel yr^{-1} in each coordinate. The separated sequence at larger errors that arises for $m_{\rm F606W} < 22.5$ is made up of stars measured only in the short exposures.

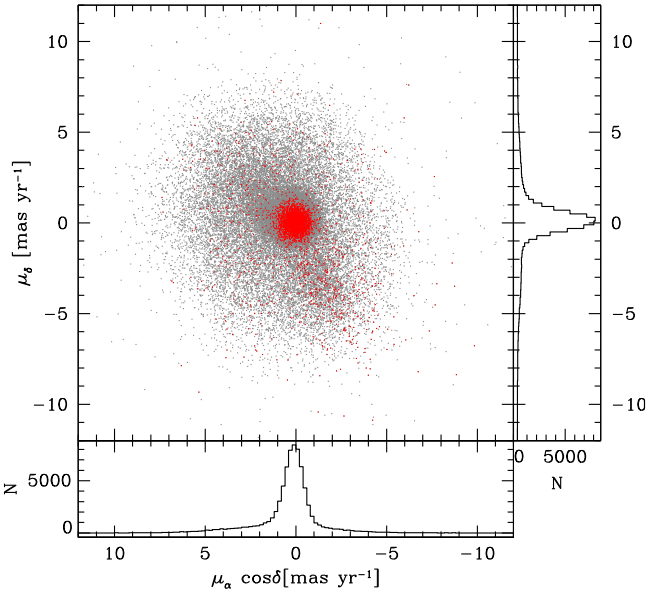

Figure 3. Vector point diagram (VPD) of the PMs measured for 70,324 stars (black dots) in the direction of Terzan 5. Their distribution in the R.A. and decl. PM-component axes is shown in the histograms in the bottom and right panels, respectively. PMs measured for unsaturated stars with $m_{\rm F606W} < 24$ mag are shown as red dots. At least two components are visible: the first showing a symmetric distribution centered around the origin and an asymmetric structure roughly centered at $(-1.8, -3.5)$ mas yr^{-1}.

direction and within each epoch were computed as

$$\sigma^{X,Y}_{1,2} = \frac{\mathrm{rms}^{X,Y}_{1,2}}{\sqrt{N_{1,2}}}, \quad (1)$$

where $\mathrm{rms}_{1,2}$ is the rms of the positional residuals about the median value, and $N_{1,2}$ is the number of measurements. Therefore, the error in each PM component associated with each star is simply the sum in quadrature between the first- and second-epoch errors: $\sigma^X_{\rm PM} = \sqrt{(\sigma^X_1)^2 + (\sigma^X_2)^2}\big/\Delta T$ and $\sigma^Y_{\rm PM} = \sqrt{(\sigma^Y_1)^2 + (\sigma^Y_2)^2}\big/\Delta T$. The errors associated with the PMs of the brightest stars measured only in the short exposures were computed by adopting as positional uncertainties the typical errors determined in the long-exposure catalogs at the same *instrumental* magnitude.

We repeated the entire procedure several times in order to reach a stable number of stars in the reference list. In performing these iterations, stars were selected on the basis of the relative PMs obtained in the previous step. To be conservative, we decided to build the final PM catalog taking into account only the 69,425 unsaturated stars measured in at least three long exposures per epoch and the 899 stars brighter than the deep image-saturation limit measured in all of the short exposures that have a total uncertainty on the displacement smaller than 0.2 pixels. All of the sources that saturate in the latter images have been excluded. The typical error as a function of magnitude is shown in Figure 2. For well-exposed stars it is smaller than 0.007 pixel yr^{-1} in each coordinate. Faint stars or stars with only a few measurements show larger errors, still typically smaller than 0.02 pixel yr^{-1} (see the separated sequence in Figure 2).

3.1. The Vector Point Diagram

We converted the PMs into units of mas yr^{-1} by multiplying the measured displacements by the pixel scale of the master frame ($0\farcs05$ pixel^{-1}). Since the master frame has been oriented according to the equatorial coordinate system, the X PM component corresponds to that projected along the (negative) R.A. ($-\mu_\alpha \cos\delta$), and the Y PM component corresponds to that along the decl. (μ_δ). The output of this analysis is summarized in Figure 3, where we show the vector point diagram (VPD) for all of the stars of the final PM catalog. The first clear feature is that more than 70% of the stars are distributed within the innermost 1.5 mas yr^{-1} from the origin of the VPD (see histograms in Figure 3). The remaining fraction of stars describes a sparser and asymmetric distribution out to about 10 mas yr^{-1}. In order to highlight these features, we selected only stars with $m_{\rm F606W} < 24$, which typically have the most accurate PMs, and plotted them as red points in Figure 3. Their distribution in the VPD clearly shows at least two components. One is a symmetric distribution centered around the origin, with PM weighted mean values $\mu_\alpha \cos\delta = 0.02 \pm 0.02$ mas yr^{-1} and $\mu_\delta = -0.01 \pm 0.02$ mas yr^{-1}. The other is an asymmetric structure approximately centered around the coordinate $(\mu_\alpha \cos\delta \sim -1.8,\ \mu_\delta \sim -3.5)$ mas yr^{-1} in the VPD. The locations of these two components in the CMD clearly reveal their nature (see Figure 4). In fact, the stars of the first component (shown as blue dots in the VPD) describe the cluster evolutionary sequences in the CMD (central lower panel), with a small degree of contamination left. In contrast, the stars belonging to the asymmetric component (red dots) correspond to the blue plume in the CMD (lower right panel), which is essentially populated by young disk stars in the foreground of Terzan 5. This is further confirmed by the comparison with the prediction of the Besançon model (Robin et al. 2003) with only young ($t_{\rm age} < 7$ Gyr) Galactic disk stars

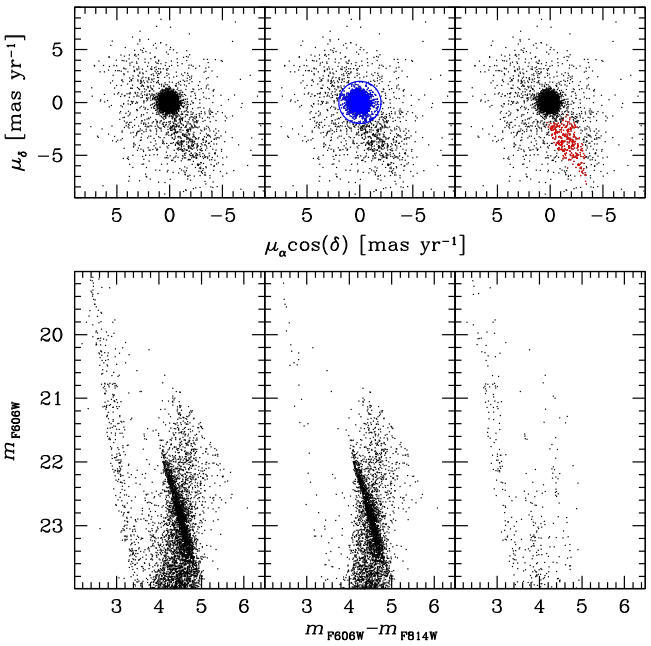

Figure 4. *Upper panels*: VPDs of all stars brighter than $m_{F606W} = 24$ mag. The PMs of stars belonging to the symmetric component of likely members are highlighted in blue in the central panel, and those of stars belonging to the asymmetric component centered at $(-1.8, -3.5)$ mas yr^{-1} are plotted in red in the right-hand panel. *Lower panels*: CMDs described by the PM-selected stars in the corresponding VPDs. When likely Terzan 5 members are selected, only the cluster evolutionary sequences are visible, with the exception of a few residual contaminating stars. In contrast, the population belonging to the asymmetric component appears to be dominated by young foreground disk stars along the blue plume.

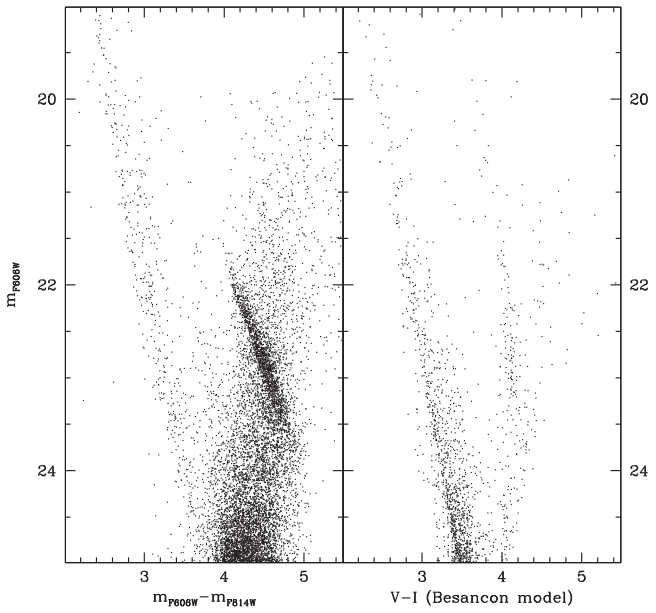

Figure 5. Comparison between the observed ACS CMD and that predicted by a simulation of the Besançon model including only Galactic disk stars younger than 7 Gyr. Such a comparison clearly demonstrates that the bluer sequence in the CMD of Terzan 5, already identified as composed of field stars by the measured PMs, corresponds to the main sequence of foreground disk stars.

for a field centered at the coordinates of Terzan 5 and covering the same FOV as that of the ACS/WFC (see Figure 5).

3.2. Check for Systematic Errors

Many systematic uncertainties may affect the measurement of relative PMs (see Bellini et al. 2014 for a detailed description). It is therefore important to check that the measured PMs of our final catalog do not suffer from such systematic effects. Since we have only two epochs of observations and a relatively small number of images per epoch (only two long exposures were acquired in the first epoch), full control of all of the possible systematics is not achievable. Nonetheless, we have carefully checked for the presence of any systematics that our data sets allow us to verify.

First of all, we looked for any possible chromatic-induced systematics by checking that no trend between PMs and color exists for our sample. Figure 6 shows the results of this test. By selecting stars in a wide magnitude range ($23 < m_{F606W} < 26$), we computed the 3σ clipped average value of our PMs (for both the spatial components) in color bins of 0.04 mag (red filled circles). The error bars are within the size of the symbols. Clearly, these values describe a flat relation (shown as a red dashed line). The best least-squares linear fit to these data gives a null angular coefficient within the uncertainty for both of the PM components. Thus, we can safely conclude that no trend with color exists for our measurements.

We repeated a similar test looking for possible trends with the observed magnitude in the range $19 < m_{F606W} < 26$ in order to exclude extremely faint sources that have intrinsically

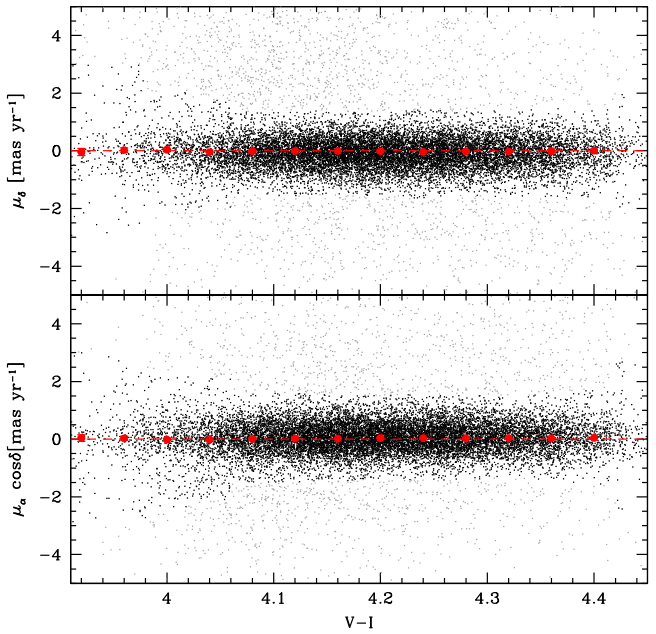

Figure 6. *Upper panel: Y* component of the relative PMs vs. observed colors. Red filled circles represent the 3σ clipped mean PMs measured in color bins of 0.04 mag. Stars rejected by the clipping algorithm are shown in gray. All of the mean values lie on the no-correlation line (red dashed line), thus excluding any chromatic-induced systematics. *Lower panel:* same as above, for the PM *X* component.

larger PM errors. Figure 7 shows the result of this test. Also in this case, the best linear fit to the 3σ clipped average PM values computed in bins of 0.3 mag is compatible (within the errors) with a null angular coefficient line, thus demonstrating that no significant trend is found with magnitude either.

Finally, we also carefully checked the existence of spurious trends with the location of stars on the detector. To do so, we followed the method described in Bellini et al. (2014), by

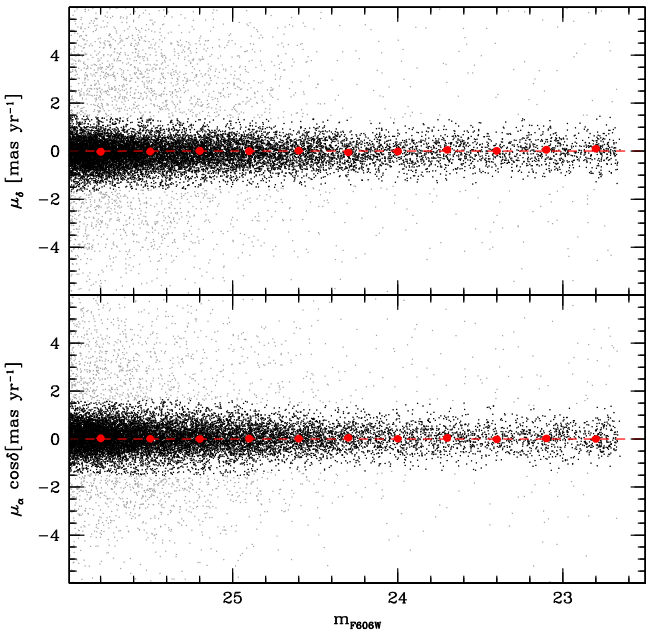

Figure 7. *Upper panel:* same plot as in Figure 6, but in terms of observed magnitude. Mean values have been computed in bins 0.3 mag wide. Also in this case, no trend is found between PMs and magnitude. *Lower panel:* same as above, for the *X* component of PMs.

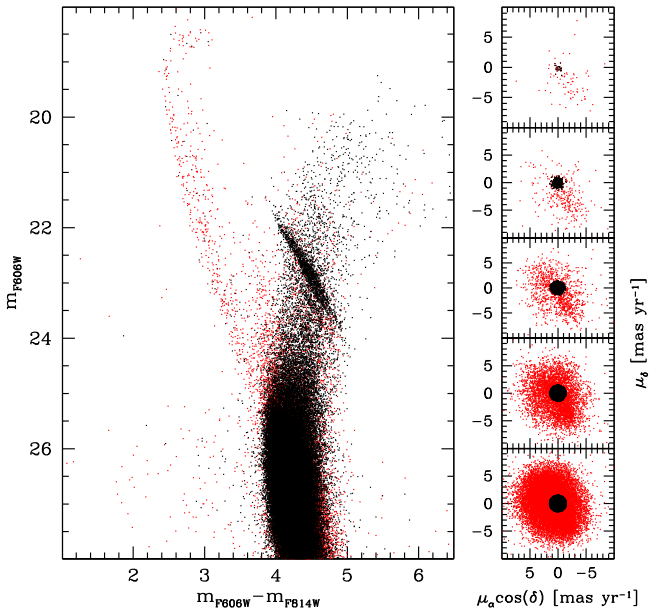

Figure 8. *Left panel:* optical CMD of Terzan 5, with likely member stars shown as black dots and field sources (excluded by the PM-based selection) plotted in red. The measured relative PMs are efficient in decontaminating the CMD, and only cluster evolutionary sequences survive the selection criterion. *Right panels:* magnitude-binned VPDs for all of the stars in the optical catalog. Each bin has a size of 2 mag. Sources are color coded as in the left panel.

plotting maps of the measured PMs as a function of the position on the sky, where to each star we associated the average motion of the closest 100 neighbors. Overall we found a homogeneous distribution in both of the PM components.

The tests discussed above demonstrate that the derived PMs do not suffer from significant systematic effects. Also, the use of available CTE-corrected images for both epochs (see Section 3) should have minimized the effect of CTE losses on the PM estimate. While we cannot exclude that other systematics can affect our measurements, we can firmly conclude that these are the best PMs we can measure with the available data set.

4. RESULTS

We used the measured relative PMs to "clean" the optical (m_{F606W}, $m_{F606W}-m_{F814W}$) CMD of Terzan 5 described in Section 2. We defined as likely member stars all of the sources located within a distance smaller than 1.5 mas yr^{-1} in the VPD plane. As shown in Figure 3, this appears to be a reasonable assumption because the bulk of the stars lie within this limit. The CMD obtained from such a selection is shown in Figure 8. Member stars are plotted as black dots, and nonmember stars are shown in red. The selection applied leaves in the CMD only stars clearly belonging to the cluster evolutionary sequences, while excluding most of the outliers. A small degree of contamination is still present because the distribution of field stars (mainly bulge stars) in the VPD overlaps that of Terzan 5 members. However, we can conclude that the PM analysis performed is efficient in decontaminating the CMD from foreground and background sources. We can therefore use this selection to assess the membership of the subpopulations discussed by Ferraro et al. (2009), Origlia et al. (2011, 2013), and Massari et al. (2014b).

4.1. MAD Infrared CMD

The two major subpopulations in Terzan 5 were identified in the (K, $J-K$) CMD by Ferraro et al. (2009). Their radial distributions are incompatible with that expected for background field stars, and the measured line-of-sight velocities are consistent with the systemic radial velocity of Terzan 5. However, the membership of the two populations has been questioned (see, e.g., Willman & Strader 2012). To address this concern and to assess their cluster membership from PMs, we cross-correlated the Multi-conjugate Adaptive optics Demonstrator (MAD) catalog with the PM catalog. The result is summarized in Figure 9. The left panel shows the IR CMD of Terzan 5 after the PM-based membership selection (black dots). The sources recognized as contaminating field stars based on the value of their PMs are also plotted in red. The decontaminated CMD clearly exhibits the two red clumps (RCs) originally discovered by Ferraro et al. (2009).

Figure 10 highlights the CMD and VPDs for subsamples of stars properly selected in the two RCs. As can be seen, the two PM distributions appear quite symmetric, both showing a small (0.5 mas yr^{-1}) dispersion around the origin. Although these PMs cannot be used to reveal possible intrinsic kinematical differences between the two populations, we can solidly conclude that these stars are all members of Terzan 5.

Overall, the number of contaminants in the IR CMD (selected as stars outside a distance of 1.5 mas yr^{-1} from the center of the VPD) is much smaller than what is observed in the optical plane. This is because the MAD photometry corresponds to a smaller FOV (with respect to the ACS one) and to the very central region of the system, where the cluster population is expected to dominate. It is also worth noticing that both of the RC subsamples are much more centrally concentrated than the likely Galactic field contaminants selected at the same magnitude level (see the red, blue, and

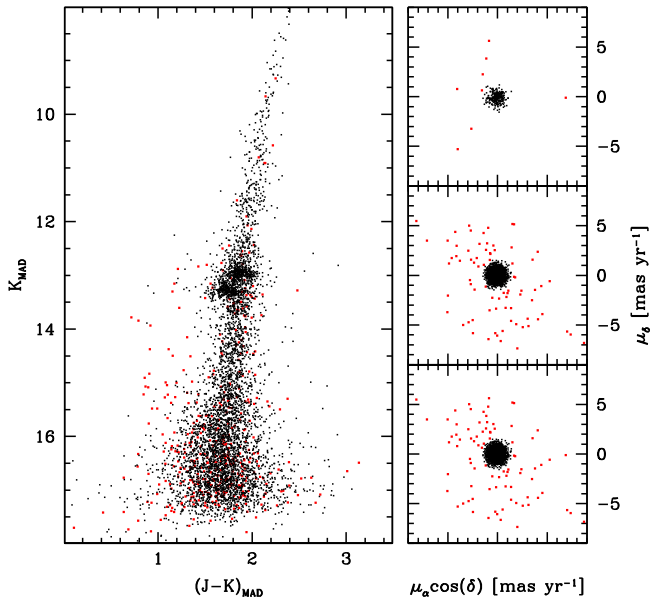

Figure 9. *Left panel:* IR CMD of Terzan 5 obtained from MAD observations. The PM-selected member stars are shown as black dots, and the sources having discordant PMs are marked in red. The presence of two distinct red clumps is well evident even after the PM-based selection. *Right panels:* magnitude-binned VPDs (each magnitude bin has a size of 3 mag). Stars are color coded as in the left panel.

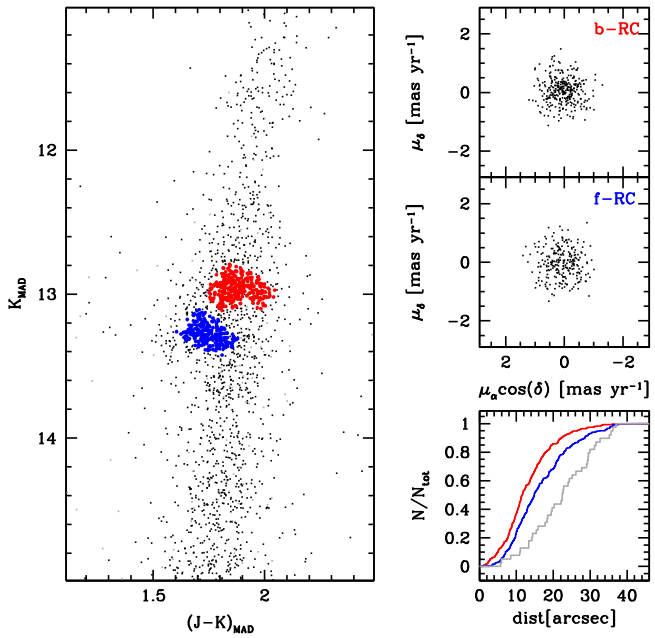

Figure 10. *Left panel:* IR MAD CMD of Terzan 5 zoomed in the RC region. Faint RC stars are plotted in blue, and bright RC stars are plotted in red. Stars rejected according to their PMs are shown in gray. *Upper- and central-right panels:* VPDs of the bright-RC and faint-RC subsamples, respectively: the stars of both populations lie within the 1.5 mas yr^{-1} circle adopted as the membership selection criterion. No clearcut difference between the two distributions is visible. *Lower-right panel*: cumulative radial distributions of bright-RC, faint-RC, and likely nonmember stars selected in the IR CMD (red, blue, and gray lines, respectively). Clearly, nonmember stars are less concentrated than cluster members, as is expected for field sources.

gray lines, respectively, in Figure 10). According to a Kolmogorov–Smirnov test performed on the three samples, the probability of PM-rejected stars having been extracted from one of the two RC populations is always smaller than 10^{-4}.

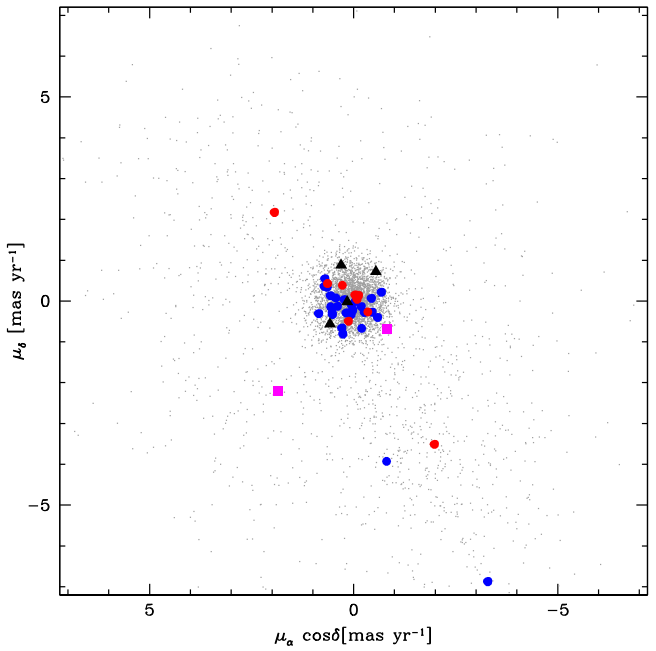

Figure 11. VPD for the spectroscopic targets discussed in Massari et al. (2014b) in common with our PM catalog. Blue circles are stars with $-0.6 \leqslant [Fe/H] < 0$, and red circles have $0 \leqslant [Fe/H] < 0.5$. These represent the two main populations of Terzan 5. Black filled triangles correspond to stars belonging to the newly discovered third, metal-poor population. All three components are clearly genuine members of the system, being located well within the PM distribution of the cluster members. The two magenta filled squares represent the super-metal-rich stars of the spectroscopic sample, and, at odds with the other sources, they seem not to belong to Terzan 5.

This further confirms that stars rejected according to our PM-membership selection are field objects, homogeneously distributed in the sampled FOV.

In conclusion, the relative PMs measured in this work and applied to the MAD CMD definitely demonstrate that the two major subpopulations photometrically discovered in Terzan 5 are both members of the system.

4.2. Spectroscopic Targets

In Massari et al. (2014b) we presented the distribution of the iron abundance for the largest sample of stars in Terzan 5. In that work, target membership was inferred from radial velocities, and the fraction of contaminating stars was estimated statistically from the chemical and kinematical characterization of the field surrounding the system itself (Massari et al. 2014a). According to that work, in the innermost 200″ the expected fraction of contaminating field stars is about 16% (18 out of 114 stars).

The measure of relative PMs gives the great opportunity to verify the membership of each single star in the ACS FOV (instead of adopting a statistical approach only) and to check whether the estimate of the contribution from contaminating stars is reliable. To this aim, we cross-correlated them with the iron abundance catalog. We found only 42 out of 135 targets in common because the majority of the spectroscopic targets are either bright RGB stars, which saturate even in the short exposures, or stars located outside the ACS FOV. The locations of these targets in the VPD are shown in Figure 11, where blue circles mark stars with $-0.6 \leqslant [Fe/H] < 0$, and red circles correspond to more metal-rich objects ($0 \leqslant [Fe/H] < 0.5$). Clearly, with only a few exceptions (four targets), all

spectroscopic targets appear to be members of the system, having PMs (and radial velocities) well within the characteristic cluster distribution. Also, four stars belonging to the newly discovered metal-poor component of Terzan 5 (with [Fe/H] $\simeq -0.8$; see Origlia et al. 2013; Massari et al. 2014b) have measured PMs and are shown in the figure (black triangles). As is apparent, they are also members of Terzan 5. Finally, the two magenta filled squares correspond to the super-metal-rich stars ([Fe/H] > 0.5) found in Massari et al. (2014b) and are suggested to be nonmembers. Indeed, their PMs are either outside the distribution of member stars or are just at its edge.

Overall, six out of 42 spectroscopic targets appear to be field stars. Such a fraction corresponds to the 14% of the sample, in very good agreement with the statistical estimate obtained from our previous spectroscopic studies. Therefore, these results confirm that the iron distribution of Terzan 5 shown in Massari et al. (2014b) is made up of genuine cluster members, showing a huge internal iron spread of more than 1 dex.

4.3. Absolute PM

One of the most intriguing applications of PM measures is the determination of the absolute motion of a stellar system. The best way is to relate the mean motion of all of the stars in the system[6] to the absolute reference frame defined by very distant objects, such as background galaxies or quasars, which appear as zero-motion sources (see, e.g., Dinescu et al. 1999; Mahmud & Anderson 2008; Bellini et al. 2010; Lépine et al. 2011; Sohn et al. 2012; Massari et al. 2013). Unfortunately, because of the high stellar density and the very large extinction in the direction of Terzan 5, we have not been able to detect such objects in the ACS FOV.

We then cross-correlated our PM catalog with many public catalogs of stellar PMs, such as NOMAD (Zacharias et al. 2005), the Guide Star Catalog version 2.3, UCAC4 (Zacharias et al. 2012), and the Yale/San Juan Southern Proper Motion catalog (Dinescu et al. 1997, Platais et al. 1998). However, because these catalogs have PMs measured only for very bright sources, we found just four stars in common with our PM sample, all having PM uncertainties larger than 8 mas yr^{-1} in the public data sets. Hence, no meaningful result about the absolute PM of Terzan 5 can be obtained from this kind of analysis.

An interesting alternative is described in Ortolani et al. (2011; see also Rossi et al. 2015), where the authors anchor the motion of the GC HP1 to that of the underlying bulge population. The bulge PM is the composition of its internal kinematics and the reflex motion of the local standard of rest (LSR). In the direction of Terzan 5, the radial velocity distribution of bulge stars peaks at $v_{\rm rad} = 21.0 \pm 4.6$ km s^{-1} (Massari et al. 2014a). Assuming that bulge stars are at the same distance from the Galactic center (here we adopt 8.4 kpc following Ghez et al. 2008 and Ortolani et al. 2011, but see also van der Marel et al. 2012 for a complete overview of the topic), the tangential component of the bulge velocity is $v_{\rm tan} = v_{\rm rad}\,\sin(l)/\cos(l) = 1.41 \pm 0.31$ km s^{-1}, or in Galactic coordinates $\mu_l^{\rm bulge} = 0.05 \pm 0.01$ mas yr^{-1}. Because the bulge shows cylindrical rotation (Howard et al. 2008; Kunder et al. 2012; Ness et al. 2013; Zoccali et al. 2014), we can assume $\mu_b^{\rm bulge} = 0$ mas yr^{-1}. By summing these values to the motion of the LSR ($\mu_l\cos(b) = 6.10 \pm 0.25$ mas yr^{-1}, $\mu_b = 0$ mas yr^{-1}, corresponding to $v_{\rm LSR} = 243 \pm 10$ km s^{-1}; see Ortolani et al. 2011), we obtain the total motion of the bulge at Terzan 5 coordinates: $(\mu_l\ \cos(b),\ \mu_b)_{\rm bulge} = (6.15 \pm 0.25,\ 0)$ mas yr^{-1}.

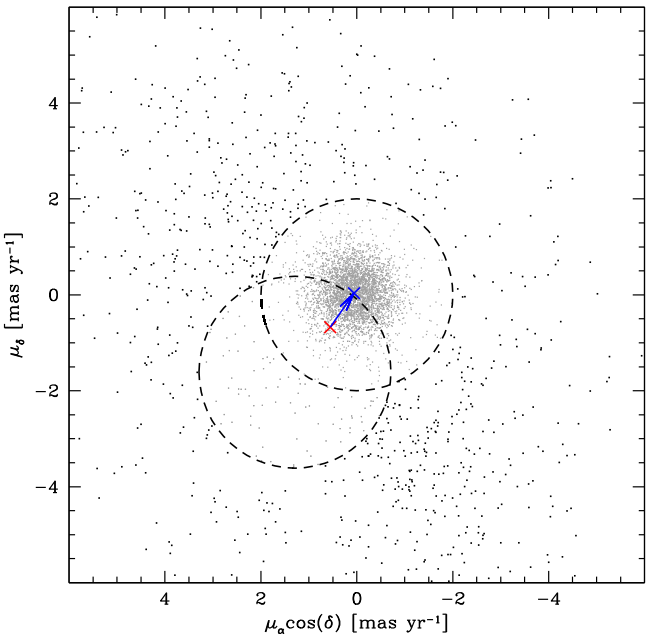

Figure 12. VPD of the sample of stars used to estimate the absolute PM of Terzan 5. The black points correspond to the bulge stars surviving the last step of the selection procedure and effectively used as reference; the gray dots mark the Terzan 5 member stars. The mean motion of the bulge sample is marked with a red cross. The PM of Terzan 5 relative to the mean bulge motion is marked with a blue arrow.

As a second step for determining the PM of Terzan 5 relative to that of the bulge, we excluded foreground disk contaminants belonging to the blue plume in the CMD by selecting a subsample of stars with $(m_{\rm F606W} - m_{\rm F814W}) > 3.9$ and $m_{\rm F606W} < 24.5$, which do not saturate even in the long exposures. We also applied a selection in terms of PM errors, by excluding stars with uncertainties larger than 0.3 mas yr^{-1} in the two PM components. We then defined as Terzan 5 members all of the stars located within 2 mas yr^{-1} from the origin of the VPD.

To select the sample of bulge stars, we followed an iterative procedure similar to that described by Anderson & van der Marel (2010) for the determination of the center of ω Centauri. After the exclusion of all Terzan 5 members, we computed the first-guess mean motion of bulge stars. We then excluded all objects contained within a circle of 2 mas yr^{-1} radius positioned at the same distance as the "Terzan 5 circle" from the first-guess mean on the symmetrically opposite side in the VPD. A new value of the mean motion has been evaluated from this sample, and the procedure has been repeated until convergence was reached. Once the Terzan 5 and the bulge samples are defined, we determined their weighted mean motion with a 3σ clipping procedure that, after the last step, included 3,853 sources for the Terzan 5 sample and 797 for that of the bulge (black dots in Figure 12). We computed the uncertainty in the weighted mean motions as the standard error in the mean, that is, the dispersion of the surviving stars around the mean PM, divided by the square root of their number.

The resulting motion of Terzan 5 relative to the bulge (see the blue arrow in Figure 12) expressed in Galactic coordinates (see Ortolani et al. 2011 for the details of the transformations)

[6] Given the large number of measured PMs, this kind of analysis usually does not require the accuracy needed to study the internal kinematics of a system.

turned out to be $(\mu_l \cos(b), \mu_b)_{\mathrm{T5-bulge}} = (0.26 \pm 0.10, 0.83 \pm 0.12)$ mas yr^{-1}, where the final uncertainties are the sum in quadrature of those computed for the two separated samples. By subtracting the motion of the bulge quoted above, we finally obtained the absolute PM of Terzan 5: $(\mu_l \cos(b), \mu_b)_{\mathrm{T5}} = (-5.89 \pm 0.27,\ 0.83 \pm 0.12)$ mas yr^{-1}, where the total uncertainties are the sum in quadrature between that coming from the motion of the bulge and that associated with the motion of the cluster relative to it. This is the first absolute PM estimate ever obtained for Terzan 5.

4.4. The Cluster Orbit

On the basis of the absolute PM estimate derived in the previous section, we performed a numerical integration of the orbit of Terzan 5 in the Galactic potential. We used the three-component (bulge, disk, and halo) axisymmetric model from Allen & Santillan (1991), which has been extensively used and discussed in the literature to study orbits and dynamical environmental effects on Galactic stellar systems (e.g., Allen et al. 2006; Montuori et al. 2007; Ortolani et al. 2011; Moreno et al. 2014; Zonoozi et al. 2014), thanks to its relative simplicity and fully analytic nature. We adjusted the various model parameters to make the rotation velocity curve match the value of 243 km s^{-1} measured at the Solar Galactocentric distance of 8.4 kpc (see above). The cluster PMs were reported in the Cartesian Galactocentric reference frame, resulting in a velocity vector $(v_x, v_y, v_z) = (-60.4 \pm 1.3, 85.7 \pm 11.1, 35.0 \pm 6.0)$ km s^{-1} at the position $(x, y, z) = (-2.51 \pm 0.30, 0.39 \pm 0.02, 0.17 \pm 0.01)$ kpc. We adopted the convention in which the X axis points opposite to the Sun (i.e., the Sun position is (−8.4,0,0)). The orbit was then time-integrated backwards for 12 Gyr, starting from the given initial (current) conditions and using a second-order leapfrog integrator (e.g., Hockney & Eastwood 1988) with a rather small and constant time step (∼100 kyr, corresponding to $\sim 1/300$ of the dynamical time at the Sun distance, computed as $(R_0^3/GM_g)^{1/2}$, where $M_g \sim 1.7 \times 10^{11} M_\odot$ is a characteristic Galactic mass parameter). During the $>10^5$ time steps used to describe the entire orbit evolution, the errors on the conservation of both the energy and the Z component of angular momentum were kept under control and never exceeded one part over 10^5 and 10^{13}, respectively. To take into account the uncertainties on the kinematic data, we generated a set of 1,000 orbits starting from the phase-space initial conditions normally distributed within a 3σ range around the cluster velocity vector components and the current position, with σ being equal to the quoted uncertainties on these parameters. For all of these orbits we repeated the backward time integration. The probability densities of the resulting orbits projected on the equatorial and meridional Galactic planes are shown in Figures 13 and 14, respectively. Darker colors correspond to more probable regions of the space, that is, to Galactic coordinates crossed more frequently by the simulated orbits. As is apparent, the larger distances reached by the system during its evolution are $R = 3.5$ kpc and $|Z| = 1.6$ kpc at a 3σ level of significance, which roughly correspond to a region having the current size of the bulge.

In a forthcoming study, we plan to quantify the possible influence of a central nonaxisymmetric component (the bar or the spiral arms). Indeed, although triaxial potentials are expected to facilitate the onset of very radial orbits (because of the lack of conservation of any angular momentum component) with a possible prolongation of the system orbital

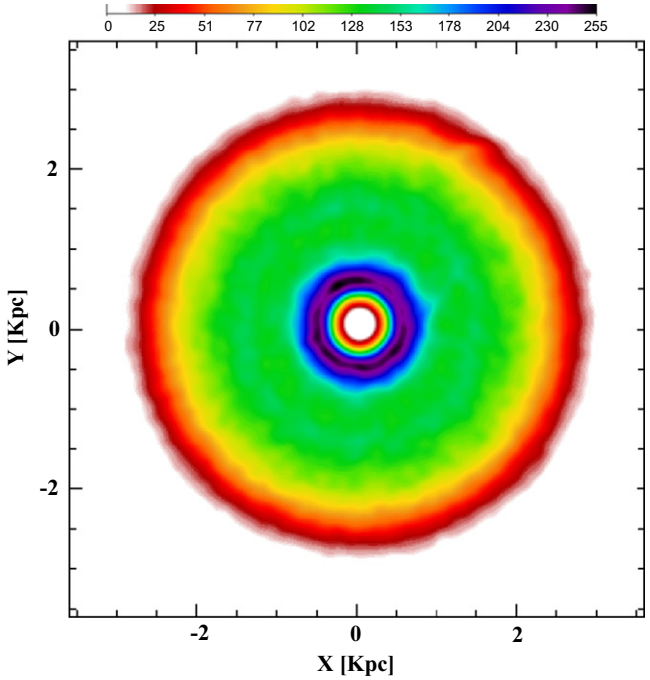

Figure 13. Probability density in the equatorial Galactic plane of 1,000 simulated orbits of Terzan 5 time-integrated backwards for 12 Gyr. Darker colors correspond to larger probabilities.

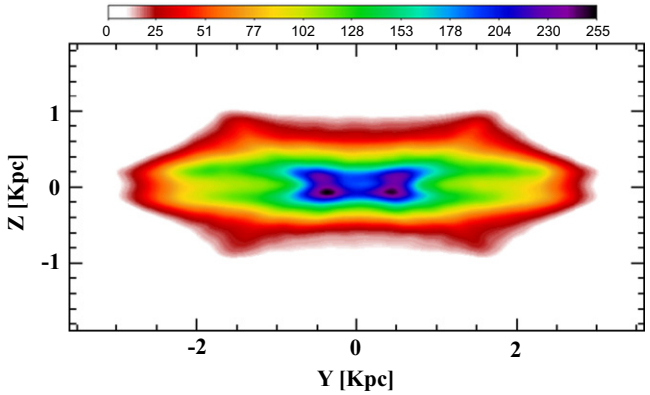

Figure 14. As in Figure 13, but for the orbit projection in the meridional Galactic plane.

motion in much farther out regions, a recent study by Moreno et al. (2014) demonstrated (using a sophisticated and realistic model) how this intuitive picture could be wrong, due to the complex interplay between the gravitational potentials generated by the various components. The relatively small perigalactic distance (<500 pc) that Terzan 5 could have achieved during its orbit could imply a significant mass loss due to tidal erosion and thus represents a further strong motivation for studying in more detail the dynamical history of this system.

Based on the current results, we can conclude that the integration of the Terzan 5 orbit performed by means of this simple axisymmetric Galactic static model suggests an in situ formation for the cluster within the Galaxy, rather than an external accreted origin. This supports the interpretation (Ferraro et al. 2009) of this system as the remnant of one of the massive stellar clumps that may have contributed to forming the Galactic bulge (Noguchi 1999; Immeli et al. 2004).

5. CONCLUSIONS

By using high-resolution ACS/WFC images, we have measured relative PMs in the direction of the stellar system Terzan 5. We have been able to separate cluster members from foreground disk stars and background bulge contaminants. The PM-selected CMD clearly confirmed that the two main populations with distinct iron content discovered in Terzan 5 are genuine members of the system, thus putting to rest this issue that had remained a matter of debate. Moreover, the measured PMs demonstrate that the third, metal-poorer and α-enhanced population also clearly belongs to the system. Our findings therefore confirm that Terzan 5 is, together with ω Centauri (Norris & Da Costa 1995; Pancino et al. 2000; Origlia et al. 2003; Johnson & Pilachowski 2010; Villanova et al. 2014), the stellar system with the largest internal iron spread in the Galaxy.

Finally, by comparing the motion of Terzan 5 members to that of bulge stars, we estimated for the first time the absolute PM of this system, finding $(\mu_l \cos(b), \mu_b)_{T5} = (-5.89 \pm 0.10, 0.83 \pm 0.12)$ mas yr^{-1}. The backward integration of its orbit, computed under the assumption of an axisymmetric Galactic model, provides another indication that supports the scenario according to which Terzan 5 is the remnant of one of the primordial stellar clumps that may have contributed to forming the Galactic bulge, and not an object accreted from outside the Milky Way.

We thank the anonymous referee for his or her useful comments that helped us to improve our paper. The authors are also grateful to Dr. Lucie Jílková for her valuable suggestions on the cluster orbit integration. This research is part of the project Cosmic-Lab (website: http://www.cosmic-lab.eu) funded by the European Research Council (under contract ERC-2010-AdG-267675). D.M. thanks the Kapteyn Astronomical Institute for hospitality. R.M.R. acknowledges support from AST-1413755 from the National Science Foundation. The techniques applied in the present work have been developed in the context of the HSTPROMO collaboration[7] (Bellini et al. 2014; van der Marel et al. 2014), which aims to improve our understanding of the dynamical evolution of stars, stellar clusters, and galaxies in the nearby universe through the measurement and interpretation of PMs.

REFERENCES

Allen, C., Moreno, E., & Pichardo, B. 2006, ApJ, 652, 1150
Allen, C., & Santillan, A. 1991, RMxAA, 22, 255
Anderson, J. 2007, Instrument Science Report ACS 2007-08
Anderson, J., & Bedin, L. R. 2010, PASP, 122, 1035
Anderson, J., & King, I. 2006, STScI Inst. Sci. Rep. ACS 2006-01 (Baltimore, MD: STScI)
Anderson, J., King, I. R., Richer, H. B., et al. 2008, AJ, 135, 2114
Anderson, J., & van der Marel, R. P. 2010, ApJ, 710, 1032
Bellini, A., Anderson, J., van der Marel, R. P., et al. 2014, ApJ, 797, 115
Bellini, A., Bedin, L. R., Pichardo, B., et al. 2010, A&A, 513, A51
Carretta, E. 2014, ApJL, 795, L28
Dalessandro, E., Ferraro, F. R., Massari, D., et al. 2013, ApJ, 778, 135
Dalessandro, E., Lanzoni, B., Ferraro, F. R., et al. 2008, ApJ, 677, 1069
Dinescu, D. I., Girard, T. M., & van Altena, W. F. 1999, AJ, 117, 1792
Dinescu, D. I., Girard, T. M., van Altena, W. F., Mendez, R. A., & Lopez, C. E. 1997, AJ, 114, 1014
Ferraro, F. R., Clementini, G., Fusi Pecci, F., & Buonanno, R. 1991, MNRAS, 252, 357
Ferraro, F. R., Dalessandro, E., Mucciarelli, A., et al. 2009, Natur, 462, 483
Ferraro, F. R., Fusi Pecci, F., & Buonanno, R. 1992, MNRAS, 256, 376
Ghez, A. M., Salim, S., Weinberg, N. N., et al. 2008, ApJ, 689, 1044
Hockney, R. W., & Eastwood, J. W. 1988, Computer Simulation Using Particles (New York: Hilger)
Howard, C. D., Rich, R. M., Reitzel, D. B., et al. 2008, ApJ, 688, 1060
Immeli, A., Samland, M., Gerhard, O., & Westera, P. 2004, A&A, 413, 547
Johnson, C. I., & Pilachowski, C. A. 2010, ApJ, 722, 1373
Kunder, A., Koch, A., Rich, R. M., et al. 2012, AJ, 143, 57
Lanzoni, B., Dalessandro, E., Ferraro, F. R., et al. 2007, ApJL, 668, L139
Lanzoni, B., Ferraro, F. R., Dalessandro, E., et al. 2010, ApJ, 717, 653
Lépine, S., Koch, A., Rich, R. M., & Kuijken, K. 2011, ApJ, 741, 100
Mahmud, N., & Anderson, J. 2008, PASP, 120, 907
Massari, D., Bellini, A., Ferraro, F. R., et al. 2013, ApJ, 779, 81
Massari, D., Mucciarelli, A., Dalessandro, E., et al. 2012, ApJL, 755, L32
Massari, D., Mucciarelli, A., Ferraro, F. R., et al. 2014a, ApJ, 795, 22
Massari, D., Mucciarelli, A., Ferraro, F. R., et al. 2014b, ApJ, 791, 101
Montuori, M., Capuzzo-Dolcetta, R., Di Matteo, P., Lepinette, A., & Miocchi, P. 2007, ApJ, 659, 1212
Moreno, E., Pichardo, B., & Velázquez, H. 2014, ApJ, 793, 110
Ness, M., Freeman, K., Athanassoula, E., et al. 2013, MNRAS, 432, 2092
Noguchi, M. 1999, ApJ, 514, 77
Norris, J. E., & Da Costa, G. S. 1995, ApJ, 447, 680
Origlia, L., Ferraro, F. R., Bellazzini, M., & Pancino, E. 2003, ApJ, 591, 916
Origlia, L., Massari, D., Rich, R. M., et al. 2013, ApJL, 779, LL5
Origlia, L., Rich, R. M., Ferraro, F. R., et al. 2011, ApJL, 726, L20
Ortolani, S., Barbuy, B., Momany, Y., et al. 2011, ApJ, 737, 31
Pancino, E., Ferraro, F. R., Bellazzini, M., Piotto, G., & Zoccali, M. 2000, ApJL, 534, L83
Platais, I., Girard, T. M., Kozhurina-Platais, V., et al. 1998, AJ, 116, 2556
Robin, A. C., Reylé, C., Derrière, S., & Picaud, S. 2003, A&A, 409, 523
Rossi, L. J., Ortolani, S., Barbuy, B., Bica, E., & Bonfanti, A. 2015, MNRAS, 450, 3270
Sohn, S. T., Anderson, J., & van der Marel, R. P. 2012, ApJ, 753, 7
Ubeda, L., & Anderson, J. 2012, STScI Inst. Sci. Rep. ACS 2012-03 (Baltimore, MD: STScI)
van der Marel, R. P., Anderson, J., Bellini, A., et al. 2014, in ASP Conf. Ser. 480, Structure and Dynamics of Disk Galaxies, ed. M. S. Seigar & P. Treuthardt (San Francisco, CA: ASP), 43
van der Marel, R. P., Fardal, M., Besla, G., et al. 2012, ApJ, 753, 8
Valenti, E., Ferraro, F. R., & Origlia, L. 2007, AJ, 133, 1287
Valenti, E., Ferraro, F. R., & Origlia, L. 2010, MNRAS, 402, 1729
Villanova, S., Geisler, D., Gratton, R. G., & Cassisi, S. 2014, arXiv:1406.5069
Watkins, L. L., van der Marel, R. P., Bellini, A., & Anderson, J. 2015, ApJ, 803, 29
Willman, B., & Strader, J. 2012, AJ, 144, 76
Zacharias, N., Finch, C. T., Girard, T. M., et al. 2012, yCat, 1322, 0
Zacharias, N., Monet, D. G., Levine, S. E., et al. 2005, yCat, 1297, 0
Zoccali, M., Gonzalez, O. A., Vasquez, S., et al. 2014, A&A, 562, A66
Zonoozi, A. H., Haghi, H., Küpper, A. H. W., et al. 2014, MNRAS, 440, 3172

[7] For details see the HSTPROMO home page at http://www.stsci.edu/~marel/hstpromo.html